Romer, *Breviora* 156, 1 (1962); O. Reig, *Ameghiniana* 3, 3 (1963)].
13. D. J. Bottjer and D. Jablonski, *Palaios* 3, 540 (1988).
14. M. J. Benton, *New Sci.* 7, 9 (1983).
15. P. N. Stipanícic, in *The Phanerozoic Geology of the World: The Mesozoic*, M. Moullade and A. E. Nairn, Eds. (Elsevier, New York, 1983), vol. 2B, pp. 188–199. Relative-abundance data are needed for the pollen and macrofloral records to address fully this question.
16. J. F. Bonaparte, *J. Vertebr. Paleontol.* 2, 362 (1982).
17. Percentages were calculated from a total sample of 238 specimens (228 specimens documented in Fig. 2 plus nine specimens mentioned in caption of Fig. 2 plus a single specimen of *Pisanosaurus*).
18. Tetrapod fossils typically occur as isolated skeletons or articulated skeletal components (limbs, vertebral segments, and skulls) in fine-grained overbank facies. Additional observations on the taphonomy of the Ischigualasto Formation can be found in R. R. Rogers *et al.*, *Fifth North Am. Paleontol. Conv. Abstr. Prog.* 249 (1992).
19. Analytical procedures follow (*28*) and references therein. The sanidine was treated with dilute (~0.7%) hydrofluoric acid for 5 min. to remove any altered glass and adhering clays and was then rinsed for 5 min. in distilled water. The sanidine was then irradiated together with a centrally located monitor mineral (Fish Canyon Tuff sanidine) for 14 hours in the Omega West research reactor at Los Alamos National Laboratory. After irradiation, single crystals of the monitor mineral and approximately 25 crystals of the Herr Toba sanidine were loaded into individual 2-mm-diameter wells of a copper sample disk and then placed within the sample chamber of the extraction system and baked out at 200°C for 8 hours. Incremental heating and total fusion of the samples and monitor mineral were accomplished with a 6-W coherent Ar-ion laser. The laser beam was not focused so that it would heat the sample wells evenly. Each well was also incrementally heated for 45 s by stepwise increases in the laser output. Purification of the released gases and data reduction are as in (*28*). The Ca and K corrections for this study, as determined from laboratory salts, are $(^{36}Ar/^{37}Ar)_{Ca} = 2.582 \times 10^{-4} \pm 6.0 \times 10^{-6}$, $(^{39}Ar/^{37}Ar)_{Ca} = 6.7 \times 10^{-4} \pm 3.0 \times 10^{-5}$, and $(^{40}Ar/^{39}Ar)_K = 2.03 \times 10^{-2} \pm 4.0 \times 10^{-4}$. A value of 0.011294 ± 0.00001 for the fluence-calibration parameter *J* was based on eight replicate single-crystal analyses of the monitor mineral Fish Canyon sanidine with an age of 27.84 Ma. The age of the Fish Canyon sanidine adopted in this study is similar to that recommended by G. T. Cebula *et al.* [*Terra Cognita* 6, 139 (1986)] but is slightly modified as a result of intercalibration with MMhb-I (Minnesota hornblende monitor mineral) with an age of 520.4 ± 1.7 Ma [S. D. Samson and E. C. Alexander, *Chem. Geol. Isot. Geosci. Sect.* 66, 27 (1987)]. Mass discrimination during this study, as determined by replicate air aliquots delivered from an on-line pipette system, was 1.005 ± 0.002. Decay constants are those recommended by R. H. Steiger and E. Jäger [*Earth Planet. Sci. Lett.* 36, 359 (1977)] and G. B. Dalrymple [*Geology* 7, 558 (1979)].
20. Plateau definition basically follows R. J. Fleck *et al.*, *Geochim. Cosmochim. Acta* 41, 15 (1977).
21. S. C. Forster and G. Warrington, in *The Chronology of the Geological Record*, N. J. Snelling, Ed. (Geological Society, London, 1985), pp. 99–113; J. W. Cowie and M. G. Bassett, *Episodes* 12 (no. 2), (suppl.) (1989); W. B. Harland *et al.*, *A Geologic Time Scale 1989* (Cambridge Univ. Press, New York, 1990).
22. A. G. Fischer, in *Cycles and Events in Stratigraphy*, G. Einsele, W. Ricken, A. Seilacher, Eds. (Springer-Verlag, New York, 1991), pp. 48–62; S. M. Kidwell, *Geol. Rundsch.*, in press. Sedimentation rates used are low to moderate for a rift basin setting.
23. P. E. Olsen and H.-D. Sues, in *The Beginning of the Age of Dinosaurs*, K. Padian, Ed. (Cambridge Univ. Press, New York, 1988), pp. 321–351.
24. Arguments for an end Carnian or late Carnian tetrapod extinction event are based on counts of families and species that have last appearances in the Tuvalian substage of the late Carnian [M. J. Benton, *Hist. Biol.* 5, 263 (1991)]. Our data suggest that the Ischigualasto taxa *Trialestes*, *Ischigualastia*, *Scaphonyx*, *Exaeretodon*, *Pisanosaurus*, and *Proterochampsa*, until now placed in the latter half of the Tuvalian, are in fact older. Thus, our results diminish the apparent magnitude of the purported end Carnian extinction event by reducing the number of last appearance events known in the Tuvalian.
25. P. A. Murry and R. A. Long, in *Dawn of the Age of Dinosaurs in the American Southwest*, S. G. Lucas and A. P. Hunt, Eds. (New Mexico Museum of Natural History, Albuquerque, NM, 1989), pp. 29–64; J. M. Parrish, in *ibid.*, pp. 360–374.
26. By guild we imply a group of organisms that utilize a common resource in a similar fashion [R. B. Root, *Ecol. Monogr.* 37, 317 (1967)]. No direct competition is implied.
27. P. C. Sereno, *J. Vertebr. Paleontol.* 11, 168 (1991).
28. C. C. Swisher III *et al.*, *Science* 257, 954 (1992).
29. Isolated skeletons or skeletal components were counted as one individual. If several fossils were found in close proximity on a single bedding plane, we determined the minimum number of individuals with methods reviewed in C. Badgley, *Palaios* 1, 328 (1986).
30. W. D. Sill, *Mus. Comp. Zool. Bull.* 146, 317 (1974).
31. The uncertainties associated with the individual incremental apparent ages are 2σ errors, whereas those that accompany the calculated weighted mean ages of the plateau increments and weighted means of the replicate analyses are standard errors (SE), following J. R. Taylor, *An Introduction to Error Analysis* (Oxford Univ. Press, New York, 1982).
32. We thank J. Alroy, M. Benton, D. Jablonski, T. Jordan, S. Kidwell, K. Roy, and N. Shubin for comments and suggestions and C. Abraczinskas for drafting the illustrations. We also thank all members of the joint Argentine-American field crews of 1988 and 1991 (O. Alcober, A. Arcucci, R. Gordillo, D. Herrera, C. May, F. Novas, W. Stevens, and C. Yu). Supported by grants from the David and Lucile Packard Foundation, the Petroleum Research Fund of the American Chemical Society, the National Geographic Society, the National Science Foundation (to P.C.S.), and the Institute of Human Origins (C.C.S.).

7 January 1993; accepted 29 March 1993

Copernicus: A Regional Probe of the Lunar Interior

Patrick C. Pinet, Serge D. Chevrel, Patrick Martin

Earth-based telescopic spectral imaging techniques were used to document the spatial distribution of crater materials within the large lunar crater Copernicus at the subkilometer scale on the basis of spectral ultraviolet–visible–near-infrared characteristics. The proposed spectral mixing analysis leads to a first-order mapping of the impact melt material within the crater. Olivine was detected not only within the three central peaks but also along a significant portion of the crater rim. Consideration of an olivine-bearing end-member in the mixing model emphasizes the overall morphological pattern of the rim and wall terraces in the associated fraction image. The identification of widely exposed olivine units supports the idea that the lower crust and possibly the lunar mantle itself are regionally at shallow depth.

Large impact craters such as Copernicus excavate materials from different depths and thus provide information at the target site on the preimpact stratigraphy and mineralogical heterogeneities of the lunar crust, both laterally and vertically (*1–3*). The recent Galileo lunar flyby revealed that the stratification of the lunar crust may be regionally affected by the presence of cryptomaria, especially on the western farside and nearside (*4*). However, the global multispectral information retrieved from the solid-state imaging (SSI) experiment onboard the Galileo spacecraft was limited in both spatial and spectral resolution, precluding any detailed geological analysis of morphological surface units such as impact craters. New Earth-based remote-sensing techniques have allowed powerful investigations of the nature and layering of the lunar crust by means of spectro-imaging analyses. In this report, we document the spatial distribution of crater materials within Copernicus at the subkilometer scale on the basis of their spectral ultraviolet (UV)–visible (VIS)–near-infrared (NIR) characteristics and compare these data with the results of previous spot-spectroscopic investigations (*1, 2, 5*).

We carried out an extensive Earth-based spectral mapping (UV-VIS-NIR domain) of Copernicus (93 km in diameter) with charge-coupled device (CCD) images that had high spatial (0.7 km) and spectral (wavelength/band pass = $\lambda/\Delta\lambda$ = 100) resolution. The observations were carried out in the September 1989 full-moon period, with a Thomson CCD camera mounted at the focus of the 2-m aperture (focal length/diameter = 25) telescope of the Pic-du-Midi Observatory (France) (*6, 7*), under 6° and 19° of phase angle, during two successive photometric nights (excellent atmospheric stability and less than 30% hygrometry). The optical configuration corresponds to a theoretical spatial sampling of 0.17 km per pixel at the subterrestrial point.

UPR 234/Centre National de la Recherche Scientifique, Groupe de Recherche en Geodésie Spatiale, Observatoire Midi-Pyrénées, Toulouse 31400, France.

The data processing (6–8) produced a high-quality, three-dimensional spectral data set. Each pixel of the image is characterized by its spectrum, retrieved from the imaging data set, and ranging from 0.4 to 1.05 μm (9); the resulting true spatial resolution available within Copernicus is then 0.7 km (Fig. 1). We then interpreted the spectral information in the light of high-resolution orbital pictures (for example, Fig. 2). The NIR (0.9 to 1.05 μm) part of the spectrum was particularly well analyzed (7, 9) and provided information on the mineralogy of the lunar crust. Absorption features related to the presence of mafic silicates (pyroxenes, olivine) occur in this spectral domain (10).

Following preliminary work (7) in which our SSI data were compared with earlier reflectance spectra (2, 5), we used the F2 spot (2) (Fig. 2) as a standard area and produced, from our imaging data set, reflectance spectra relative to F2 and scaled to unity at 0.73 μm (Fig. 3). A general consistency (within 1 to 2% mean deviation), both in terms of overall continuum slope and absorption features, was found with earlier spectra available for particular spots (Fig. 2) (2). In particular, our data show that all three central peaks exhibit a broad absorption band near 1.05 μm (Fig. 3) which, as found earlier (1, 2), indicates olivine as the major mafic component. There exists a variation in the band strength within a factor 2 to almost 3 among the three peaks, with the easternmost peaks (Pk3 and Pk2) being the most absorbent.

On the basis of this agreement (7, 9), we then produced a detailed spectromineralogical map of the Copernicus interior and its surroundings, by applying a spectral mixing analysis based on the end-member technique (11, 12) to the F2 relative reflectance spectra (13). Such an analysis applied to Copernicus shows that a mixing of three components can account for nearly all the total spectral variance of the image. Once the olivine-bearing lithology end-member (Pk3 area) is selected, the two most distinct end-members within the image in terms of UV-VIS-NIR relative reflectance are produced by the EJ1 and EJ2 end-members. These correspond to the external southwestern rim and northwestern rim of the crater, respectively (Figs. 3 and 4) (14).

In contrast to the albedo maps, the overall morphology of the rim and wall terraces of the crater is conspicuously visible in the fraction images, particularly in the Pk3 fraction image (Fig. 4A). The present survey agrees with the recent identification, at lower spatial resolution, of olivine-rich areas along the northern wall, both by NIR imaging (15) and by thermal infrared spectra (16). Consistent with these independent identifications (15, 16), at least the areas mapped in red and white (Fig. 4A) must have a significant olivine-rich content. Consequently, we propose that olivine is the primary mafic component, not only within the three central peaks (1–3) but also along the rim and wall terraces of the crater.

The end-member analysis also reveals that a significant amount of material with consistent spectral features is distributed across the crater floor, discontinuously spread on the northern walls and terraces, and that it covers, within the available mapping, a large area in the northwestern part of the outer crater rim, where the EJ2 end-member occurs (Fig. 4B). A third kind of terrain, mainly represented by the EJ1 end-member and locally containing an EJ2-like component, extends continuously within the southwestern quadrant of the image (Fig. 4C). This unit covers the outer part of the rim and locally contributes to the surface material on the southwestern walls and terraces of the crater. Its spectral

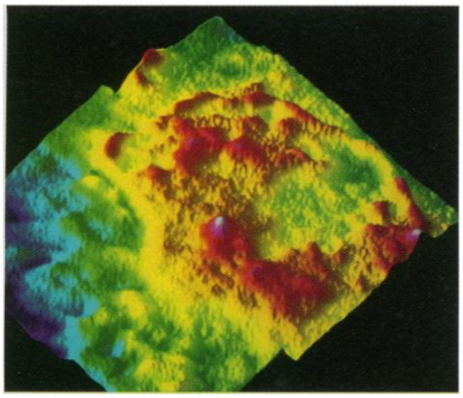

Fig. 1. Three-dimensional representation of an Earth-based telescopic mosaic of the interior of Copernicus crater produced from two 0.73-μm images. The brightness contrast of crater features observed at high spatial resolution (~500 m) is displayed, ranging from dark blue (low intensity) to white (high intensity). Peaks and walls appear bright. North orientation is at the upper right corner.

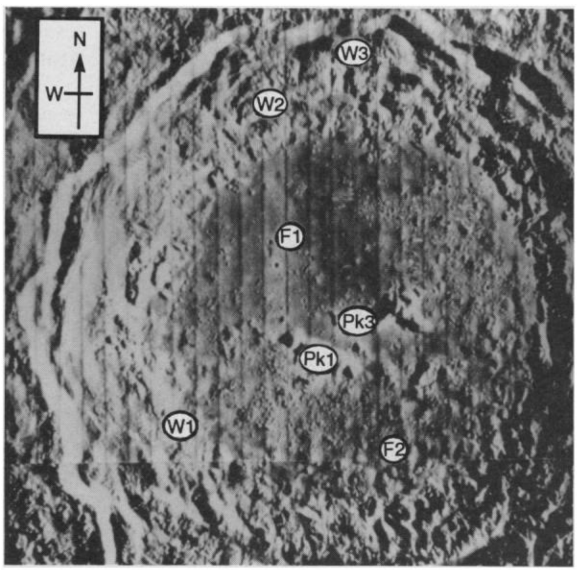

Fig. 2. Lunar Orbiter V vertical view (V-151-M) of Copernicus crater. Shown are locations of areas observed by NIR spot spectroscopy (1–3, 5).

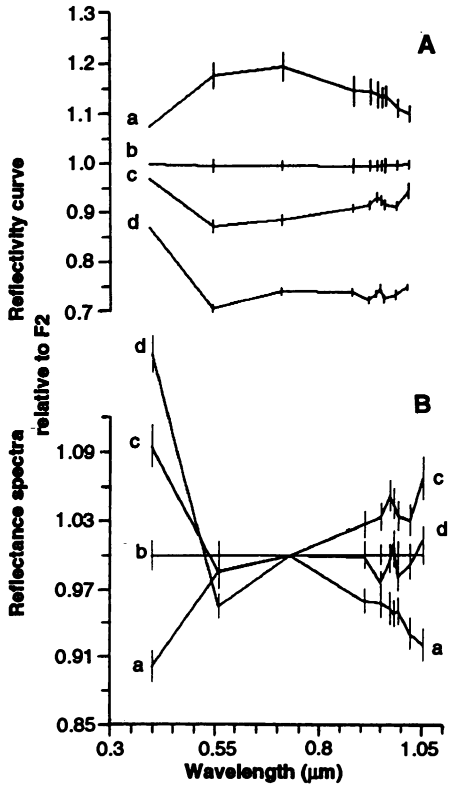

Fig. 3. The UV-VIS-NIR (0.4 to 1.05 μm) spectral characteristics relative to F2 (see text) of the selected end-members Pk3, EJ1, and EJ2. (**A**) Reflectivity curves relative to F2 with a 5% variation interval; a, b, c, and d correspond, respectively, to Pk3, F2, EJ2, and EJ1 curves. (**B**) Corresponding reflectance spectra relative to F2, scaled to unity at 0.73 μm with a 3% variation interval.

properties differ from those of the material constituting the floor and the interior of Copernicus, and its UV-VIS slope might be characteristic of mare-like material (Fig. 3).

The above results provide information on the production of impact melt generated at the time of the crater formation and on the regional geological setting of the crust in the Copernicus region. Copernicus is about 0.8 billion years old (*17*). On the basis of the lunar impact cratering chronology, it formed near the end of the lunar bombardment history, when the impact flux had substantially decreased, and ulterior impact cratering (Copernican period) was modest (*18*). By 1 billion years ago, the lunar interior had significatly cooled and the lithosphere was thick enough that any craters were preserved against morphological modification as a result of isostatic relaxation of the topography (*19*). As a result, the initial impact morphology for Copernicus has been retained, with the possible exception of the development of some inner rim block slumpings (*20*). In addition, the type, amount, and spatial distribution of materials distributed across the crater should be directly representative of the regional preimpact crustal stratigraphy of the target and of the generation and emplacement of materials related to the impact processes during the formation of a 100-km lunar crater.

In the past, the nature of the terrain in large craters like Copernicus has been mainly inferred from high-resolution orbital images. On these photogeological grounds, it was proposed that the lava-like materials that pond in the floor depressions, wall terraces, and parts of the rim of several large craters were impact melts (*21–23*). More recently, this notion has been reinforced by means of remote-sensing observations at specific locations (*5*), such as F1 and W2 (see Fig. 2). Our images identify extended units within Copernicus (Fig. 4B) that have spectral characteristics consistent with these spots, suggesting that these units are an extensive impact melt sheet. In addition, the spectral features of these units represented by the EJ2 spectrum (Fig. 3B) indicate a slope increase (reddening effect) in the domain from 0.7 to 1.05 μm, an overall albedo drop as seen on the reflectivity curve relative to F2 (Fig. 3A), and an obvious slope change in the UV range (Fig. 3B).

All of these features are consistent with optical alteration effects due to melting and vitrification processes, as seen in laboratory spectra (*24*). On the basis of spectral evidence, the EJ2 fraction image (Fig. 4B) provides a first-order mapping of the impact melt component at Copernicus. This reveals that vast areas (green and red-toned in Fig. 4B) are spectrally homogeneous and similar to EJ2. It also indicates that an impact melt contribution is present, in variable proportion, in the image (white and violet tones in Fig. 4B), forming over a wide area an irregular annulus around the peak complex. In addition, the observed spectral homogeneity suggests that the impact melt ejecta are identical inside and outside the crater rim. However, the exact melt amount present in the soil is not yet known because the proposed linear spectral mixing may not account properly for the optical alteration due to melt generation.

As seen in the end-member fraction images (Fig. 4), most of the interior and immediate surroundings of the crater can be described, on the kilometer scale, as a linear combination of either ejecta-like material (with a variable amount of impact melt) or mare-like material and olivine-bearing rocks, in variable proportion. The presence of the olivine component (Pk3 end-member) on the inner walls (Fig. 4A) along the slumped rim blocks (Fig. 2) leads to the proposition that we are identifying along the inner walls olivine-rich ejecta, which originated from the greatest depth of the crater transient cavity. The ejecta are detected on the scarps formed by failure of the rim during crater modification, because that portion of the ejecta overturned flap is well exposed. On the basis of the 0.56 μm/0.73 μm multispectral ratio, this material appears to be immature and may be freshly exposed because it occurs along steep portions of the rim (Fig. 2). Under this interpretation, the three central peaks, a significant portion of the northeastern rim, and, to a lesser extent, much of the rim and wall material would then include material from deep stratigraphic horizons. It also suggests that the floor material surrounding the peaks and the olivine-rich material detected on the inner part of the rim originated at a similar depth. Reconstruction of the transient cavity for a lunar crater the size of Copernicus suggests that the depth of the cavity below the original ground surface is on the order of 7 to 9 km (*25, 26*). It is worth noting that many local areas of the floor exhibit a spectrally significant olivine contribution (white spots in Fig. 4A) as seen at the site of the small crater, close to spot F1 (Fig. 2) and possibly piercing the overlying horizons, and in some hummocky areas.

In our spectro-imaging technique, the observing conditions and the spatial resolu-

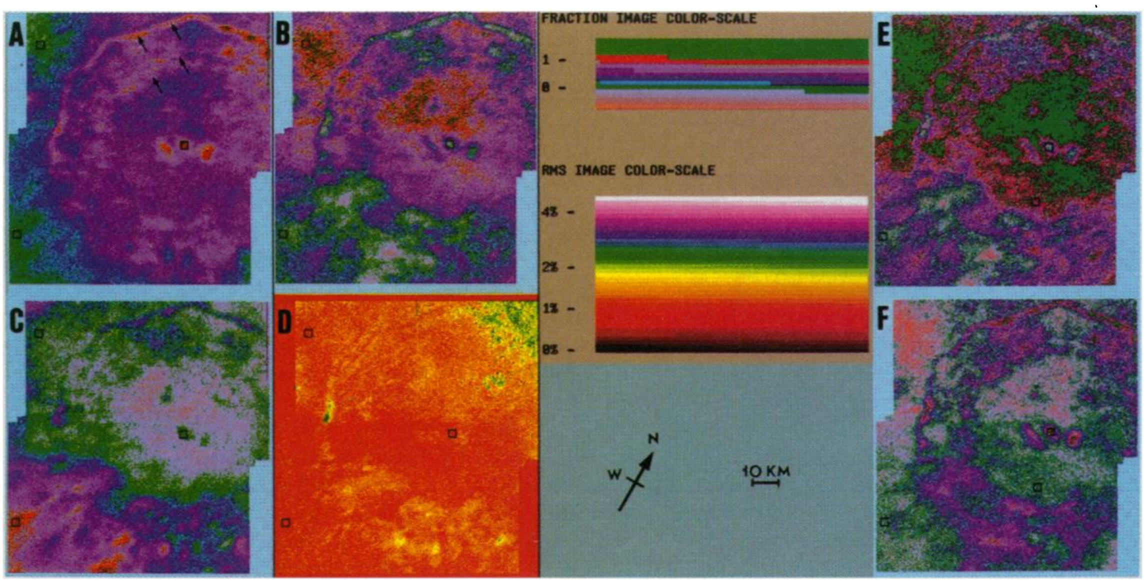

Fig. 4. Spectromixing analysis of Copernicus crater with the selected Pk3, EJ1, EJ2, and F2 end-member spectra (see Fig. 3). End-member locations are represented by open squares. (**A** to **C**) The Pk3, EJ2, and EJ1 end-member fraction images, respectively. Color coding of fraction value f is as follows: pale pink for $f < -0.1$; dark green for $-0.1 < f < 0.1$; blue for $0.1 < f < 0.2$; dark blue for $0.2 < f < 0.4$; violet for $0.4 < f < 0.6$; light violet for $0.6 < f < 0.8$; white for $0.8 < f < 0.9$; red for $0.9 < f < 1.1$; and green for $f > 1.1$. Arrows in (A) point to the olivine-rich locations identified in (*15*). (**D**) Residual standard deviation image. Color-coding ranges from black (0%) to violet (4%). (**E** and **F**) The F2 and Pk3 end-member fraction images when, in the previous ternary mixing, F2 is taken instead of EJ2. The EJ1 fraction image and the residual standard deviation image are nearly unchanged.

tion are rigorously the same for every image pixel. Consequently, under the reasonable assumption, supported by the analysis of the 0.56 μm/0.73 μm multispectral ratio, that the three peak units are in the same physical and optical alteration states, the absorption variation detected within the peaks (Fig. 4A) reflects their modal abundance of olivine. Peaks Pk3 and Pk2 are the most absorbing peaks and are spectrally homogeneous at the subkilometer scale. The formation of the central peaks of large complex craters (*27*) results from the uplift of deep-seated strata. The possibility that peak Pk2 is stratified has been inferred from high-resolution photogeology (*28*). Given the spatial extent (~5 km by 5 km) and the spectral homogeneity of the Pk2 unit, this scenario would require the uplifting of deep-seated material of uniform composition through a substratum several kilometers thick. The depth of origin for the peaks (*29, 30*) is estimated to be about 10 km.

Our results then suggest that the petrology of the target was uniform throughout the stratigraphic horizons from which the rim and peak materials originated, possibly corresponding to 1 to 3 km in thickness (*25, 26, 29, 30*). Consequently, the preimpact target had an olivine-bearing lithology at shallower depth than previously thought (*2*).

The proposed mixing model reveals that the F2 spectrum can be described as a linear combination of the UV-VIS-NIR characteristics of the EJ2 and Pk3 spectra (Fig. 3B). As verified with another ternary mixing model, which takes F2 instead of EJ2 as an end-member, the spatial distribution of the compositional unit spectrally identical to F2 (Fig. 4E) corresponds to the violet areas in both Figs. 4A and 4B. This shows that F2 is representative of the material distributed on the crater floor and underlying the discontinuous impact melt sheet (green-toned in Fig. 4E). The F2 unit is also found on the walls and outside the rim, where it is not obscured by the melt, mare-like, or olivine-rich deep-seated ejecta (Fig. 4, E and F). This proves that F2 is representative of the material constituting the upper stratigraphic horizons of the target substratum. On the basis of previous reflectance spectroscopic observations, the F2 spectrum is considered to be characteristic of an upper crustal noritic composition (*1, 2, 31*). These horizons should thus have a significant pyroxene-bearing lithology, but the fact that the F2 spectrum can be described as a mixing of EJ2 and Pk3 end-members suggests that there may also be an olivine component (*32*) whose proportion increases downward within these horizons.

Although the linear mixing approach is generally not appropriate for interpretations in terms of mineralogic abundance, we question whether the W2, W3, W1, F2, Pk1, and Pk3 observed spectra (*2, 5, 31*) might not support the idea of a target lithology with a progressive change in the pyroxene/olivine ratio with depth (*32*). The observed distribution of EJ2-like and F2-like units (Fig. 4E) agrees well with previous observations (*5, 31*) indicating locally the presence of substantial amounts of pyroxene in the ejecta. Indeed, the impact melt ejecta-like material within Copernicus, represented by the F1 spectrum (Fig. 2) (*5*), might have, depending on its degree of melting, spectral properties intermediate between those of the EJ2 and the F2 spectra. In addition, the F2 spectral characteristics might also be affected by the melting-recrystallization process. The exotic bumpy shapes (<3%) around 0.95 μm of the EJ2 and EJ1 spectra relative to F2 (Fig. 3B) might be due to the spectral features of the standard (F2) combined with an optical alteration effect related to melting-recrystallization processes (*24*). Such an unexplained bump was also observed in previous spectra W2 and F1 (*5*).

The mare-like material (EJ1) constitutes a consistent unit (Fig. 4C) located southwest of Copernicus and mixed with an F2- and EJ2-like component (Fig. 4, B and E). This unit would represent ejecta from a near-surface horizon of the target associated with basaltic Eratosthenian flows (*33*). Alternatively, the low-albedo unit represented by EJ1 might be a dark mantle deposit tapped by the impact (*31*). In the proposed stratigraphy of the target, the overlying horizons (Imbrium ejecta and mare basalt) would then have a typical thickness of <1 km.

The spectro-imaging approach used here is a relatively small step in the development of new investigative tools, but it may yield a quantitative leap in the amount of new information if a spectro-imaging experiment can fly aboard a lunar orbiter. Such an experiment would address many geological questions concerning the still poorly understood structure and mineralogy of the lunar crust. The case of Copernicus, however well documented by orbital photogeology and reflectance spot spectroscopy, illustrates that one can still gain significant insight both into the understanding of crater formation and related impact melt generation processes and into the regional composition of the unknown underlying crustal setting. On the basis of earlier studies (*30, 34, 35*), additional work on our data should provide quantitative constraints on the mechanics and melt production related to the impact cratering process. The spectral properties and the spatial distribution of the units identified by the above spectro-mixing analysis lead to a stratigraphic mode at the Copernicus target site. It is composed of near-surface thin mare basalt and noritic ejecta layers overlying a substratum whose lithology has a varying pyroxene-olivine proportion (*32*). Its spectral characteristics are less and less dominated by pyroxene at lower depths. The most olivine-rich material (Fig. 4F) (peak material Pk2 and Pk3) and deep-seated olivine-rich deposits widely exposed on the inner walls) originate from the deepest horizon of the target sampled by the impact. As previously recognized (*1, 2, 36*), this indicates the presence of a troctolitic-dunitic lithology, but the amount of detected olivine-rich ejecta and the observed spectral homogeneity of the peaks suggest that the troctolitic horizon is encountered at shallower depth than previously thought.

Although it is difficult to discriminate among the various proposed hypotheses concerning the structure of the sub-Copernicus crust (*2*) and the origin of the exposed olivine units, our results favor a substantial regional thinning of the crust by repeated early basin-forming events (pre-Nectarian period) (*2, 37*). In this region, the lower crust and possibly even the mantle itself are accessible at shallow depth at the 50- to 100-km scale.

Alternatively, if the olivine-rich lithologies detected at Copernicus originate from a layered pluton or intrusion within the crust (*2, 38, 39*), our data require a large diameter for this pluton to account for the amount of olivine-rich, deep-seated material detected in the crater. If the preimpact Copernicus target was a mafic layered pluton, one has to take into account that little spectral variation is observed across the blocky Pk2 and Pk3 units at the subkilometer scale and that this may correspond to an original compositional homogeneity at a depth of several kilometers below the Copernicus target.

REFERENCES AND NOTES

1. C. M. Pieters, *Science* **215**, 59 (1982).
2. _____ and D. E. Wilhelms, *J. Geophys. Res.* **90** (*Proc. Lunar Planet. Sci. Conf. 15*), C415 (1985).
3. C. M. Pieters, *Rev. Geophys.* **24** (no. 3), 557 (1986).
4. M. J. S. Belton *et al.*, *Science* **255**, 570 (1992).
5. S. Smrekar and C. M. Pieters, *Icarus* **63**, 442 (1985).
6. P. C. Pinet and S. Chevrel, *J. Geophys. Res.* **95**, 14435 (1990).
7. S. Chevrel, P. C. Pinet, O. Lesbre, *Lunar Planet. Sci.* **XXII**, 201 (1991).
8. S. Chevrel and P. C. Pinet, *Proc. Lunar Planet. Sci. Conf.* 22, 248 (1992).
9. P. C. Pinet, S. Chevrel, P. Martin, *Lunar Planet. Sci.* **XXIII**, 1075 (1992).
10. J. B. Adams, *J. Geophys. Res.* **79**, 4829 (1974).
11. _____, M. O. Smith, A. R. Gillespie, *Proc. IEEE Int. Geosci. Remote Sensing Symp.* **I**, 16 (1989).
12. _____, in *Remote Geochemical Analysis: Elemental and Mineralogical Composition*, C. M. Pieters and P. Englert, Eds. (Univ. of Cambridge Press, New York, in press).
13. In this approach, we used a linear mixing model to evaluate the distribution of spectroscopically dis-

tinct materials across the crater. On the basis of previous Lunar Orbiter and Apollo photogeological information and statistical tests of their spectral properties, we selected small areas (~3 km by 3 km) with both high internal spectral homogeneity and distinct respective spectral behavior to define an end-member basis in the image. Each pixel can then be represented by the fraction of each end-member taken in the linear combination that minimizes the difference between the model and the actual pixel spectrum. It is then possible to produce (i) a standard deviation image revealing the units that are not satisfactorily described by the proposed model and (ii) fraction images relative to each end-member. The end-member fractions are constrained to sum to 1.0, but each fraction may range out of the interval [0,1].

14. With such a ternary model, the residual mean standard (rms) deviation is ≈1% with $s_{rms} < 1\%$ for 51% of the pixel population, and most of the unexplained variance is concentrated in local parts of the image. This case may mean that additional end-members are needed locally. However, the residual is already close enough to the limit expected from our signal-to-noise ratio performance estimate because the rms image mimicks the boundary between the two basic pictures constituting the mosaic with a residual slightly less than 1% (Fig. 4D). This model brackets the fractions of the maximum (45%) of image pixels within the interval [0, 1], the minimum and maximum EJ1, EJ2, and Pk3 fraction values ranging, respectively, between [−1.1, 1.2], [−1.7, 2.4], and [−0.3, 1.7].
15. P. G. Lucey, B. R. Hawke, K. Horton, *Geophys. Res. Lett.* **18**, 2133 (1991).
16. A. L. Sprague *et al.*, *Icarus* **100**, 73 (1992).
17. P. A. Eberhardt, A. Stettler, J. Geiss, N. Grosler, *Moon* **8**, 104 (1973).
18. F. Hörz, R. Grieve, G. Heiken, P. Spudis, A. Binder, in *Lunar Source Book*, G. H. Heiken *et al.*, Eds. (Univ. of Cambridge Press, New York, 1991), pp. 61–120.
19. J. L. Hall, S. C. Solomon, J. W. Head, *J. Geophys. Res.* **86**, 9537 (1981).
20. J. W. Head, *Moon* **12**, 299 (1975).
21. K. A. Howard and H. G. Wilshire, *J. Res. U.S. Geol. Surv.* **3**, 237 (1975).
22. B. R. Hawke and J. W. Head, in *Impact and Explosion Cratering: Planetary and Terrestrial Implications*, D. J. Roddy *et al.*, Eds. (Pergamon, New York, 1977), pp. 815–841.
23. K. A. Howard, *U.S. Geol. Surv. Map I-840* (1975).
24. B. E. Clark, F. P. Fanale, J. W. Salisbury, *Icarus* **97**, 288 (1992).
25. C. F. Chyba, *ibid.* **92**, 217 (1991).
26. M. Settle and J. W. Head, *J. Geophys. Res.* **84**, 3081 (1979).
27. R. J. Pike, *Icarus* **43**, 1 (1980).
28. P. H. Schultz, *Moon Morphology* (University of Texas, Austin, 1976).
29. M. R. Dence, R. A. F. Grieve, P. B. Robertson, in *Impact and Explosion Cratering: Planetary and Terrestrial Implications*, D. J. Roddy *et al.*, Eds. (Pergamon, New York, 1977), pp. 247–275.
30. D. J. Roddy, in *ibid.*, pp. 185–246.
31. C. M. Pieters *et al.*, *J. Geophys. Res.* **90**, 12393 (1985).
32. R. B. Singer, *ibid.* **86**, 7967 (1981).
33. J. L. Whitford-Stark and J. W. Head, *ibid.* **85**, 6579 (1980).
34. R. A. F. Grieve, M. R. Dence, P. B. Robertson, in *Impact and Explosion Cratering: Planetary and Terrestrial Implications*, D. J. Roddy *et al.*, Eds. (Pergamon, New York, 1977), pp. 791–814.
35. R. A. F. Grieve and J. W. Head, *J. Geophys. Res.* **88**, A807 (1983).
36. C. M. Pieters, S. F. Pratt, J. M. Sunshine, *Lunar Planet. Sci.* **XXI**, 962 (1990).
37. E. A. Whitaker, *Proc. Lunar Planet. Sci. Conf.* **12A**, 105 (1981).
38. G. Ryder, *Geophys. Res. Lett.* **18**, 2065 (1991).
39. C. M. Pieters, *ibid.*, p. 2129.
40. This research was supported by the French National Program of Planetology of the Institut National des Sciences de l'Univers and the Centre National de la Recherche Scientifique. We acknowledge the support of the Pic-du-Midi Observatory staff during observations with the 2-m telescope, with special thanks to P. Caumette, J. P. Lafforgue, J. M. Lavie-Cambot, F. Lacassagne, C. Duthu, and P. Dhérété for their dedicated work. We thank C. M. Pieters for providing the F2 relative reflectance spectra, which allowed a comparison between earlier spectroscopic observations and our CCD imaging data. We also appreciate the reviews and constructive comments by J. W. Head and an unidentified reviewer, which improved the discussion significantly.

14 October 1992; accepted 18 February 1993

Sequences and Structures Required for Recombination Between Virus-Associated RNAs

Pamela J. Cascone,* Tarik F. Haydar, Anne E. Simon†

RNA recombination has been described for a number of viruses in the plant and animal kingdoms, but the mechanisms of selection of recombination sites are poorly understood. The nonrandom recombination between two subviral RNAs associated with turnip crinkle virus was used to study the requirement for specific sequences and structures in the generation of recombinant molecules. Single-base mutations that disrupted either the stem or the loop of one of the two computer-predicted stem-loop structures eliminated detectable recombinant molecules. However, recombinants were detected if compensatory mutations were generated that re-formed a stable hairpin structure. These results provide evidence for the necessity of specific structures in the formation of recombinant molecules in this system.

The exchange of genetic material, as has been demonstrated for a growing number of plant and animal viruses, may be important in the evolution, repair, and diversification of viral genomes (*1*). Most of the evidence suggests that viral RNA recombination involves a copy choice mechanism whereby the viral replicase switches from one template to an alternate location on the same or a different template where polymerization of the nascent strand then continues (*2*). An examination of intertypic poliovirus recombinants (*3*) and recombinants between genomic RNAs of the tripartite brome mosaic virus (*4*) has led to the suggestion that local regions of hybridization are the preferred sites for template switching in these systems. However, the availability of many favorable recombination sites in poliovirus and brome mosaic virus genomes and the apparently random nature of RNA recombination in most other viral systems (*5*) have precluded a detailed analysis of how the replicase, nascent strand, and templates interact to generate recombinant molecules.

Turnip crinkle virus (TCV), a monopartite, single-stranded RNA virus, is naturally associated with both defective interfering (DI) RNAs (*6*) and recombinant molecules derived from combining a linear satellite (sat-) RNA and the 3′ region of the viral genomic RNA (*7, 8*). One of three ~20-nucleotide (nt) consensus sequences, two of which are similar to sequences at or near the 5′ ends of TCV-associated RNAs, is always located at the right side of the crossover junctions (*8, 9*). These findings led us to propose a replicase-driven, copy choice mechanism for RNA recombination during synthesis of plus-strands (*9*).

An unusual example of aberrant homologous recombination between two TCV subviral RNAs has also been found (*9*). The parental RNAs were sat–RNA D (194 bases), a sat-RNA of unknown origin without appreciable sequence similarity to the viral genomic RNA, and sat–RNA C (356 bases), a molecule originally formed from two recombination events between sat–RNA D and the TCV genome (Fig. 1). Recombinant molecules appear to be precisely joined at one of five bases in sat–RNA C (positions 175 to 179), with 30% of the molecules also containing nontemplate-encoded nucleotides at the crossover point (*9*). The five bases at the junctions of the recombinants are contained within a larger 19-base sequence (motif I) in sat–RNA C (positions 175 to 193) that is similar to the junction sequence in one TCV DI RNA, as well as to a sequence near the 5′ terminus of the TCV genomic RNA.

To determine the role of motif I in recombination between sat–RNA D and sat–RNA C, we constructed a variant of sat–RNA C (deletion of nts 57 to 78) that could only be amplified in plants after recombination with sat–RNA D (*10*). Transcripts containing mutations in and

Program in Molecular and Cellular Biology and the Department of Biochemistry and Molecular Biology, University of Massachusetts, Amherst, MA 01003.

*Present address: Department of Biology, University of California at San Diego, La Jolla, CA 92093.
†To whom correspondence should be addressed.